

Thermal expansion of unidirectional and cross-ply fibrous monoliths

M.Y. He^a, D. Singh^b, J.C. McNulty^a, F.W. Zok^{a,*}

^aMaterials Department, University of California, Santa Barbara, CA 93106-5050, USA

^bEnergy Technology Division, Argonne National Laboratory, Argonne, IL 60439-4838, USA

Received 24 April 2001; received in revised form 2 January 2002; accepted 2 January 2002

Abstract

An investigation of the thermal expansion behavior of ceramic fibrous monoliths (FMs) is presented. The emphasis is on the development and validation of material models applicable to $\text{Si}_3\text{N}_4/\text{BN}$ FMs in both unidirectional and cross-ply architectures. Approximate analytical models are developed for the coefficient of thermal expansion (CTE) based on the analysis of representative unit cells of the Si_3N_4 fibers and the surrounding BN interphase. The pertinent cell shapes are identified from quantitative measurements on real $\text{Si}_3\text{N}_4/\text{BN}$ FMs. Corresponding finite element analyses are performed on the same unit cells for the purpose of validating the analytical models. Good agreement is obtained between the model predictions and experimental measurements of CTE. A rudimentary modification to the analytical model to account for texturing and anisotropy of the BN appears to yield adequate results. © 2002 Elsevier Science Ltd. All rights reserved.

Keywords: A. Ceramic matrix composites; B. Thermal properties; C. Elastic properties; C. Finite element analysis (FEA); Fibrous monoliths

1. Introduction

Fibrous monoliths (FMs) comprising Si_3N_4 fibers and a BN interphase exhibit good potential for high temperature thermostructural applications. The attractive characteristics include low costs [1], reasonably high strength and high fracture toughness. The low cost is derived largely from the use of straightforward powder-processing routes, including: (i) co-extrusion of the constituent phases into green monofilaments, (ii) the formation of unitapes by filament winding, (iii) lay-up of the unitapes to produce the requisite (multidirectional) fiber architectures, and (iv) densification of the laminates through conventional hot-pressing, HIPing or pressureless sintering (see, for example, the review by Kovar et al. [2] and the references therein). Variations on this process that involve solid freeform fabrication have also shown promise for producing three-dimensional fiber architectures and component shapes and for further reducing the costs, especially those associated with the hand lay-up methods [3]. In cross-ply architectures, the strength, $\sigma_{0/90}$, in the $0^\circ/90^\circ$ loading orientation is about 250 MPa [4]

(comparable to that of conventional SiC/SiC composites with the same architecture [5]). Because of the presence of the weak BN interphase in the transverse plies, the strength is dictated by the axial plies: the inference being that the fiber strength, $\sigma_f \geq 2\sigma_{0/90} \approx 500$ MPa. The latter value is consistent with that of some monolithic Si_3N_4 materials although there may be some room for improvement through enhanced process control. Similar strength levels are obtained in the $\pm 45^\circ$ orientation ($\sigma_{45} \approx 250\text{--}300$ MPa [4]). The initiation fracture resistance of these FMs is ≈ 10 MPa $\sqrt{\text{m}}$: about 3 times the fracture toughness of neat Si_3N_4 [4]. This difference is attributable to the deflection of cracks that are in the Si_3N_4 into the BN interphase and the associated mitigating effects on the crack tip stress intensity. Subsequent to cracking of the fibers, the fracture resistance increases further with increasing crack length, a consequence of pullout of the broken fibers past the surrounding BN, and, at steady-state, reaches values of $K_{ss} \approx 20\text{--}25$ MPa $\sqrt{\text{m}}$ [4].

With the expectation that this class of FMs will find use in high temperature thermostructural applications, a further understanding of their thermo-elastic properties will be required, both for component design and for materials development. The present study addresses one aspect of this property group, notably the coefficient of thermal expansion (CTE), over a temperature range

* Corresponding author. Tel.: +1-805-893-8699; fax: +1-805-893-8486.

E-mail address: zok@engineering.ucsd.edu (F.W. Zok).

relevant to the targeted service conditions (ambient to 1200 °C). The study includes CTE measurements on unidirectional and cross-ply FMs along the principal material directions and neat specimens of both BN and Si₃N₄, all processed in the same manner. Additionally, composite models are developed to describe the CTE of the FMs in terms of the topology and the thermoelastic properties of the constituent phases. Measurements and models of elastic moduli are also included, as needed for understanding the thermal expansion behavior of the FMs. Comparisons between the experimental measurements and model predictions are made and used to draw insights regarding the utility of the models and to identify deficiencies associated with texturing of the constituents.

The paper is organized in the following way. Section 2 describes the materials and their processing history. Section 3 presents the experimental techniques and measurements. The models are detailed in Section 4. Comparisons between the model predictions and the experimental measurements are made in Section 5.

2. Materials

All materials were manufactured by Advanced Ceramics Research. The powders for the constituent phases were prepared separately and mixed with a thermoplastic binder. The fiber powder consisted of equiaxed particles of Si₃N₄, ≈0.5 μm in diameter, and small amounts of yttria and alumina powders to aid in sintering. The Si₃N₄ was primarily α-phase, with small amounts (≈5%) of β-phase [7]. The final composition was Si₃N₄-6 wt.% Y₂O₃-2 wt.% Al₂O₃. The BN powder was composed of well-crystallized HCP platelets, ~10 μm in diameter and ~0.2 μm thick. After mixing, the Si₃N₄ compound was compression molded into a 20 mm diameter rod. The BN compound was compression molded into a matching pair of split cylindrical shells, 1 mm thick and 20 mm in diameter. The BN shells were snugly fitted around the Si₃N₄ rod to make a cylindrical composite feedrod comprising a central core of the Si₃N₄ and a concentric shell of BN. The feedrod was then extruded through a heated die to create continuous 220 μm diameter green filaments, comprising a Si₃N₄ core and a thin uniform BN coating. Shear-induced re-orientation of the BN platelets results in a highly textured structure with the basal planes of the BN aligned parallel to the surface of the Si₃N₄ [7].

Green unitapes were produced by winding the filaments around a mandrel and fixing them into place with a spray adhesive. The unitapes were then cut and stacked into the desired architecture (either 0° or 0°/90°) through a hand lay-up procedure. The stacked assembly was then warm-pressed at 100–150 °C at a pressure of 2 MPa. During the warm pressing, the filaments were deformed to a shape dictated by the fiber lay-up

(described later). The thermoplastic binder was removed by heating slowly to 700 °C in a nitrogen atmosphere. The plates were then hot-pressed at 1750 °C for 2 h to a final density of ~98% of the theoretical value. This also leads to the transformation of the Si₃N₄ from α to β [7]. FM plates in both unidirectional (0°) and cross-ply (0°/90°) architectures were produced, each with dimensions of 155 mm×155 mm×3.2 mm. For comparison, plates of neat BN and Si₃N₄ were also made using the same starting powders, thermoplastic binder and sintering additives, and following the same extrusion, lay-up and hot-pressing procedures.

Quantitative metallography was employed to determine the volume fractions of Si₃N₄ and BN in the FMs as well as to characterize the cross-sectional shape of the fibers. In both the 0° and 0°/90° materials, the volume fractions of BN and Si₃N₄ were $f \approx 20\%$ and $1-f \approx 80\%$, respectively. However, the fiber shapes in these two cases were different, as described below.

In the unidirectional FM, the fibers exhibited a shape that resembles a flattened hexagonal prism (Fig. 1). This

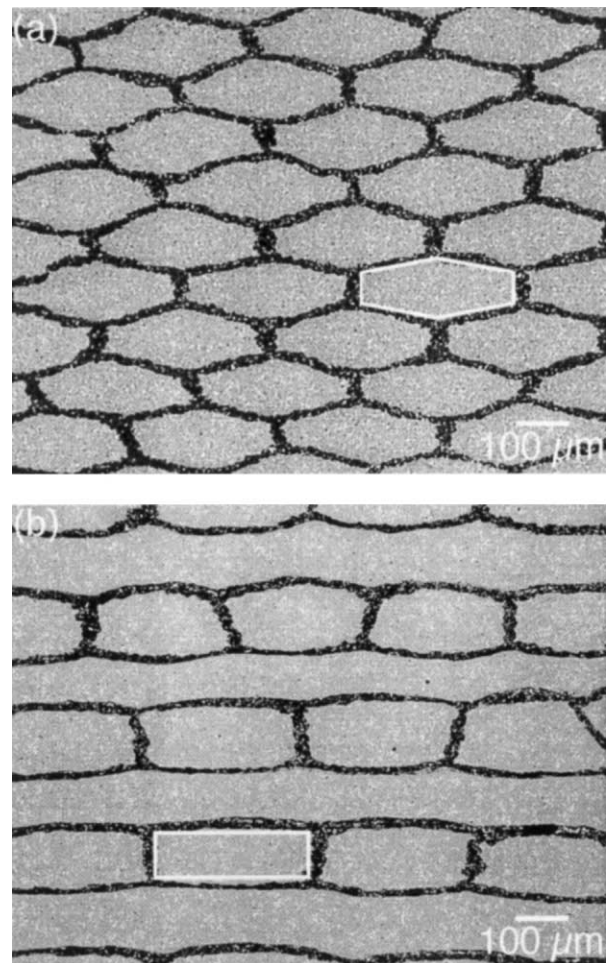


Fig. 1. SEM micrographs of cross-sections through the (a) unidirectional Si₃N₄/BN FM, and (b) cross-ply FM. The overlaid outlines are the idealized fiber shapes.

shape is a manifestation of the nearly-hexagonal packing of the green fibers in the stacked assembly coupled with the large axial compressive strains that are produced during warm pressing. A schematic of the idealized fiber cross-section is shown in Fig. 2. The cross-section is defined by a regular hexagon that has been re-scaled in the *y*-direction (defined in Fig. 2) by a factor, $k < 1$. The re-scaling reduces the length of the short sides (parallel to the *y*-direction) from 2ℓ to $2k\ell$, and the long sides from 2ℓ to $\ell\sqrt{3+k^2}$. The long and short axes of the flattened hexagon are $a = 2\sqrt{3}\ell$ and $b = 4k\ell$, and the corresponding aspect ratio, a/b , is $\sqrt{3}/2k$.

The value of k that gives the best fit of the flattened hexagon to the actual fiber shape was taken to be that which produces the combination of enclosed area, A , and perimeter, P , that correlates best with the real fibers. For this purpose, the areas and perimeters of the fibers were measured by quantitative metallography on a cross-section containing >300 fibers. The predicted values of these parameters are:

$$P = 4k\ell \left[1 + \sqrt{1 + 3/k^2} \right] \quad (1)$$

and

$$A = 6\sqrt{3}k\ell^2 \quad (2)$$

The relevant non-dimensional ratio of these parameters is

$$\frac{P}{\sqrt{A}} = a \sqrt{\frac{k}{6\sqrt{3}}} \left[1 + \sqrt{1 + 3/k^2} \right] \quad (3)$$

The distribution in the measured ratio P/\sqrt{A} is plotted in Fig. 3. Its average value is $P/\sqrt{A} = 4.44$. From Eq. (3), the scaling factor that yields the same ratio of P/\sqrt{A} is $k = 0.35$. To further demonstrate the correlation, a flattened hexagon for which $k = 0.35$ has been superimposed on the micrograph of the real fibers in Fig. 1(a).

The fibers in the cross-ply materials were essentially rectangular in cross-section [Fig. 1(b)]. In this case, no opportunity exists for nesting of fibers in adjacent laminae

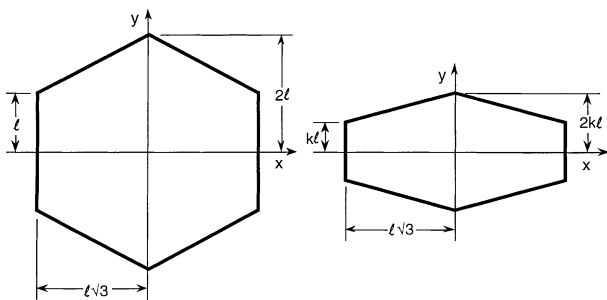


Fig. 2. Re-scaling of a regular hexagon to produce a flattened hexagon that resembles the cross-section of the Si_3N_4 fibers in the unidirectional FM.

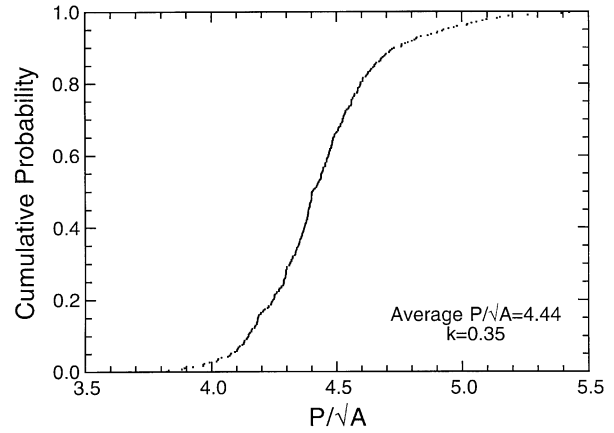


Fig. 3. Characterization of fiber shape in the unidirectional FM.

into a hexagonal arrangement (as in the unidirectional FM). Upon warm pressing, the mutual constraints of adjacent laminae give rise to a flattening of the fibers into the observed rectangular shape. The average width, a , and thickness, b , of the resultant fibers were determined from quantitative metallography measurements on > 100 fibers, yielding an average aspect ratio, $a/b = 3.4$. Again, for comparison with the real fibers, the idealized shape has been superimposed on the micrograph in Fig. 1(b).

The preceding characterizations of fiber shape were used to select appropriate unit cell shapes for the models described in Section 4.

3. Experiments

3.1. Measurement techniques

The coefficients of thermal expansion of the FMs and the neat constituents were measured using a dual-rod differential dilatometer (Model Dilatronic, Theta Industries, Port Washington, NY). The technique involves measurement of the difference of expansion between the test sample and a standard material for which the expansion is known (dense polycrystalline Al_2O_3), thereby eliminating the expansion of the system. The displacements were measured by LVDTs and the temperature profiles were measured by thermocouples; both were monitored and recorded using a computer. Periodic calibration checks of the dilatometer were made using a platinum standard sample.

Measurements of thermal expansion were made in either two or three orthogonal directions, depending on material symmetry. The neat BN and Si_3N_4 specimens are transversely isotropic; the plane perpendicular to the hot pressing direction is thermally isotropic, with a CTE that differs (in general) from the through-thickness value. Similar symmetry exists in the $0^\circ/90^\circ$ FM because of the balanced cross-ply lay-up. By contrast, the 0° FM exhibits orthotropic symmetry; the three principal directions

are: (i) parallel to the fiber direction (denoted “in-plane longitudinal”), (ii) transverse to the fibers and aligned with the plane of hot pressing (denoted “in-plane transverse”), and (iii) parallel to the hot pressing direction (denoted “through-thickness”).

The in-plane measurements were made using rectangular bars, $\approx 3 \text{ mm} \times 4 \text{ mm}$ in cross-section and 30 mm long (the long axis coinciding with the principal direction of interest). The through-thickness measurements were made using a series of stacked specimens, each $\approx 3 \text{ mm}$ thick and each polished carefully to ensure flat and parallel faces. The use of several such specimens in a stack rather than a single thin specimen increases the total displacement associated with thermal expansion and hence increases the precision in the measurements. To verify the stacking technique, some measurements were made on stacked specimens cut from the in-plane orientation and the results were then compared with the ones obtained from the long (contiguous) rectangular bars. The two sets of measurements were found to be essentially equal to one another. The measurements were made in a N_2 atmosphere during both heating and cooling over the temperature range 20–1200 °C. The heating and cooling rates were 2.5 °C/min. The results

are presented in the form of a secant CTE relative to ambient temperature, defined by:

$$\alpha = [\varepsilon(T) - \varepsilon(T_a)] / (T - T_a) \quad (4)$$

where $\varepsilon(T)$ is the thermal strain at temperature, T , and $\varepsilon(T_a)$ is the thermal strain at ambient temperature, $T_a = 20 \text{ °C}$.

The longitudinal (in-plane) elastic moduli of the FMs and the neat constituent specimens were determined in four-point flexure. The specimen dimensions were 3.2 mm \times 5 mm \times 50 mm, and the inner and outer loading spans were 15 and 40 mm, respectively. Strain gauges were bonded to the tensile and compressive surfaces within the constant moment region. The stresses were calculated using standard beam theory. The moduli were determined through linear regression of the initial (linear) part of the stress–strain curves. Three tests were performed for each material and architecture.

3.2. Experimental results

The CTE measurements on the constituents and the FMs are summarized in Fig. 4. In the neat Si_3N_4 , the

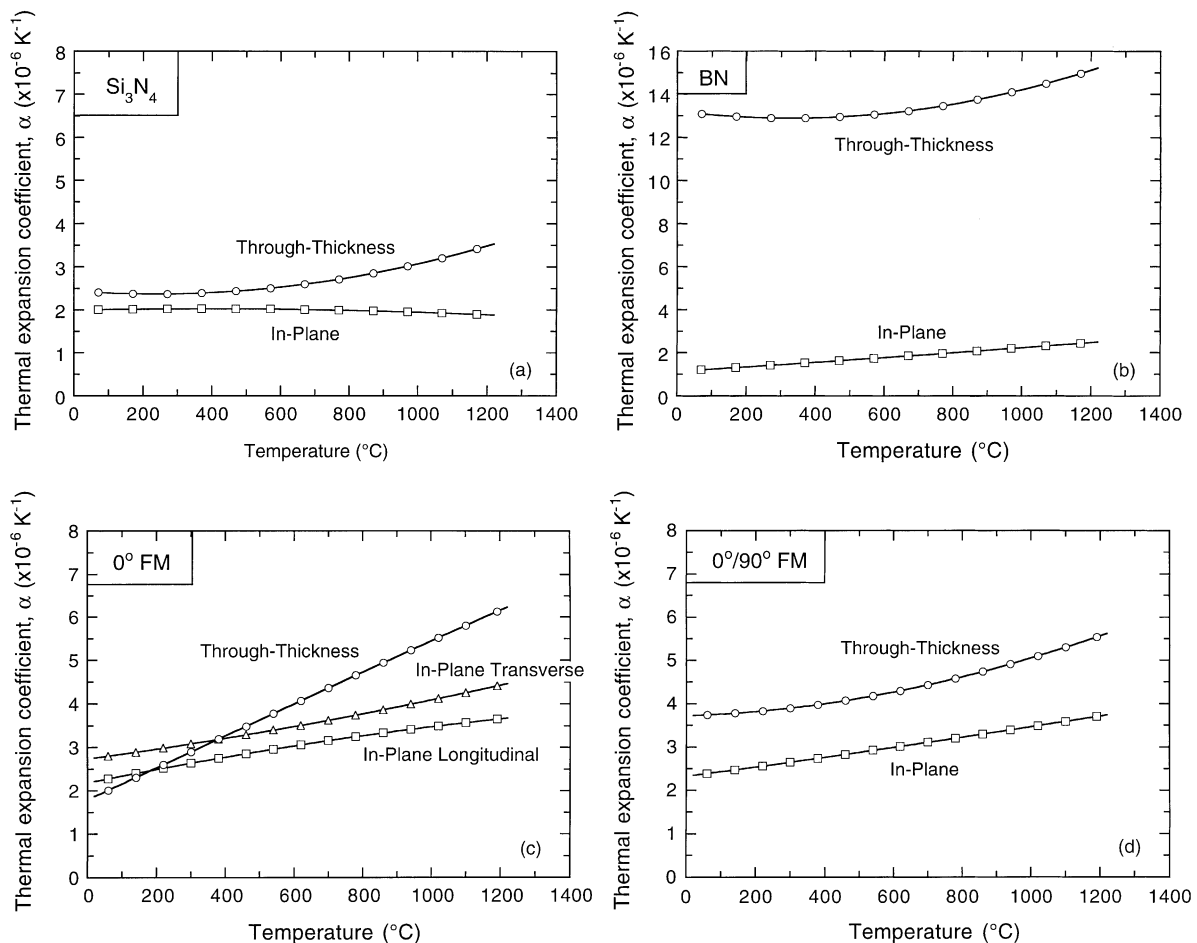


Fig. 4. Summary of CTE measurements on the neat constituents and the FMs.

in-plane CTE was almost independent of temperature. Its average value ($2.0 \times 10^{-6} \text{ K}^{-1}$) is comparable to the values reported previously for a wide range of Si_3N_4 ceramics [6]. The average through-thickness value was slightly higher: $2 \times 10^{-6} \text{ K}^{-1}$. This anisotropy is consistent with slight texturing of the hexagonal β -grains, with the basal plane oriented preferentially in the plane of hot pressing. It occurs through alignment of the pre-existing β - Si_3N_4 particles during pressing and preferred growth of the new β grains on the pre-existing β particles. [7]. The neat BN exhibited a similarly low in-plane CTE ($\approx 1.8 \times 10^{-6} \text{ K}^{-1}$), but a *much* higher through-thickness CTE ($\approx 13.5 \times 10^{-6} \text{ K}^{-1}$). Here, the anisotropy is attributed to shear-induced alignment of the hexagonal BN platelets during pressing. Similar effects have been observed within the BN phase of $\text{Si}_3\text{N}_4/\text{BN}$ FMs after extrusion, using both TEM and X-ray diffraction [7–9]. The FMs also exhibited some anisotropy in CTE, somewhat greater in magnitude than that of the neat Si_3N_4 but substantially less than that of the BN. This correlation can be rationalized qualitatively on the basis that the major constituent of the FM is Si_3N_4 and thus the behavior of the FMs should mimic that of the neat Si_3N_4 . The models and analysis presented below validate this assertion in a quantitative manner.

The relevant elastic properties are summarized in Table 1. These results are used in subsequent modeling, especially for establishing connections between the CTEs of the constituents and those of the 0° and $0^\circ/90^\circ$ FMs. A particularly notable feature is the large difference in the elastic moduli of the constituents: the modulus of the Si_3N_4 being more than an order of magnitude greater than that of the BN. A consequence is that the BN produces only minimal constraint on the thermal strain in the Si_3N_4 , especially that parallel to the fiber axis.

4. Modeling

4.1. Approach

Two complementary modeling approaches are developed to describe the CTE of the FMs. The first is based on finite element analyses (FEA) of two unit cell models, each being representative of either the unidirectional or the cross-ply FM. When combined with the appropriate

thermoelastic properties of the constituents, this approach yields essentially exact results. The second approach involves partitioning the unit cell for a unidirectional lamina (comprising a rectangular Si_3N_4 fiber and a uniform BN layer) into a convenient set of sub-cells and approximating the behavior of each of the sub-cells through standard upper or lower bound estimates for the CTE. In this way, approximate analytical solutions are obtained for the principal CTEs of the laminae within the cross-ply FM. Despite the differences in the cell geometry in the unidirectional and cross-ply materials (flattened hexagon vs. rectangle), it is demonstrated that the results obtained using the sub-cell approach for the rectangular cell (relevant to the laminae in the cross-ply FM) are also applicable to the hexagonal fiber in the unidirectional FM. The results for the individual (unidirectional) laminae are used subsequently to model the behavior of the cross-ply laminate using classical lamination theory. Comparisons are made between the analytical solutions and the exact numerical results for select cases, mainly for the purpose of validating the analytical solutions. The model predictions are compared with the experimental results in Section 5. Furthermore, a rudimentary approach to the incorporation of the anisotropy of the constituents is described and shown to produce adequate results for the through-thickness CTE.

4.2. Finite element analyses

Finite element analyses (FEA) of thermal expansion were performed on unit cells of both the unidirectional and the cross-ply FMs using the ABAQUS code. For the unidirectional FM, the fiber cross-section was taken to be a flattened hexagon, characterized by $k=0.35$. Because of the geometry and packing arrangement of the fibers, the calculations were two-dimensional. The finite element mesh for the hexagonal cell comprised 168 10-node biquadratic quadrilateral generalized plane strain elements (Fig. 5). For the cross-ply FM, three-dimensional calculations were performed using the unit cell model shown in Fig. 6. In this case, the fibers were taken to be rectangular in cross-section with an aspect ratio, $a/b=3.4$, and arranged in a two-dimensional orthogonal pattern, commensurate with the real fiber arrangement in the cross-ply FM [Fig. 1(b)]. The mesh comprised 2016 20-node quadratic brick elements and 9725 nodes. For comparison with the hexagonal cell model for the unidirectional FM, finite element calculations were also performed for a two-dimensional arrangement of the rectangular fibers, again with an aspect ratio of 3.4. The latter results demonstrate the rather weak sensitivity of the material behavior to the fiber cross-section (flattened hexagon vs. rectangle). For the CTE calculations, the surfaces of the cell boundaries were constrained to remain planar with zero shear traction and zero average

Table 1
Summary of the measured elastic moduli

Material	E (GPa)
BN	21 ± 2
Si_3N_4	242 ± 4
0° FM	216 ± 2
$0^\circ/90^\circ$ FM	181 ± 6

Values for FMs correspond to longitudinal orientation.

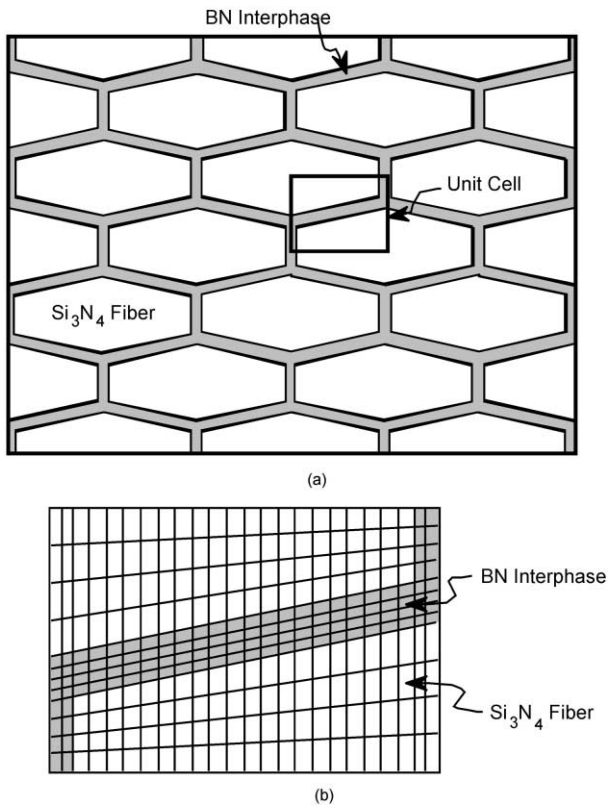


Fig. 5. (a) Schematic of the periodic array of unidirectional fibers and the associated unit cell; (b) finite element mesh of the unit cell.

normal traction. FEA of the elastic moduli of the unidirectional FMs were also performed, as needed to understand the thermal expansion behavior of the cross-ply FMs. For the latter calculations, similar boundary conditions were used with the exception that the surface normal to the loading direction had an average stress equal to the applied stress.

In all cases, the relative amounts of Si₃N₄ and BN were selected to be consistent with the respective volume fractions, $f=0.8$ and $1-f=0.2$. Both phases were

assumed to be elastic. In most cases, the Young's moduli of the constituents were taken to be those measured experimentally: $E_f=242$ GPa (for the Si₃N₄ fibers) and $E_i=20.7$ GPa (for the BN interphase). The Poisson's ratio for both phases was taken to be $\nu=0.2$. For comparison between the FEA and the analytical models, some FEA calculations were performed for a range of modulus values, characterized by the ratio $\beta \equiv E_i/E_f$.

The results from the FEA and comparisons with the analytical models are presented in the next section.

4.3. Analytical model

The longitudinal thermoelastic properties of the unidirectional FM are obtained using a standard Voigt averaging procedure, assuming the Poisson's ratios of the two constituent phases to be equal to one another. The longitudinal modulus, E_z , and thermal expansion coefficient, α_z , are given by:

$$\frac{E_z}{E_f} = f(1 - \beta) + \beta \quad (5)$$

and

$$\alpha_z = \frac{\alpha_i(1-f)\beta + \alpha_f f}{f + (1-f)\beta} \quad (6)$$

where α_i and α_f are the thermal expansion coefficients of the interphase and fiber, respectively. For the purpose of comparing the analytical solutions for the CTE with those from the finite element calculations, it is convenient to re-express the result in Eq. (6) as:

$$\alpha_z = C_{iz} \alpha_i + C_{fz} \alpha_f \quad (7)$$

where C_{iz} and C_{fz} represent the respective contributions from the interphase and fiber to the thermal expansion coefficient in the z -direction; they are:

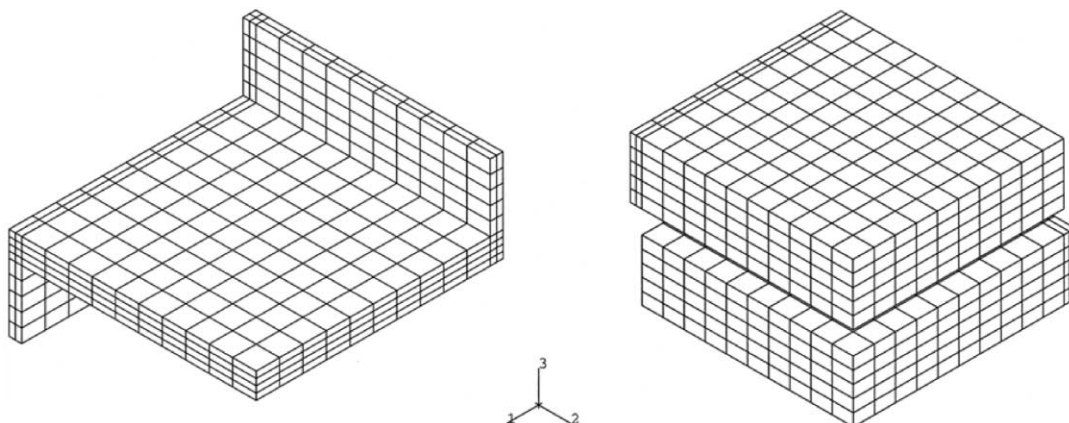


Fig. 6. Finite element mesh of the interphase (left) and the fibers (right) in the idealized cell geometry for the cross-ply FM.

$$C_{iz} = \frac{(1-f)\beta}{f + (1-f)\beta} \text{ and } C_{tz} = \frac{f}{f + (1-f)\beta} \quad (8)$$

Comparisons between the elastic modulus in Eq. (5) and that obtained from the finite calculations are shown in Fig. 7. Similarly, comparisons of the coefficients C_{iz} and C_{tz} in the CTE relationships [Eq. (8)] are shown in Fig. 8(a). In all cases, the differences are extremely small ($\ll 1\%$).

In deriving analytical expressions for the *transverse* elastic moduli and thermal expansion coefficients, the rectangular unit cell (applicable to the cross-ply FM) is first subdivided into three sub-cells: one representing the fiber and two representing the surrounding interphase material. Two such subdivision schemes are used. In the first [Fig. 9(b)], the interphase is partitioned into the two parts labeled I_1 and I_2 . A composite sub-cell is created by combining the fiber, labeled F , with the interphase sub-cell I_2 . The Young's moduli of this composite sub-cell in the x - and y -directions are evaluated using the Voigt and Reuss averages, respectively, yielding:

$$\frac{E_x^B}{E_f} = \frac{1 + \beta t}{1 + t} \quad (9a)$$

and

$$\frac{E_y^B}{E_f} = \frac{\beta(1 + t)}{\beta + t} \quad (9b)$$

where λ and t are normalized cell dimensions [defined in Fig. 9(a)] and are related to the fiber volume fraction through:

$$f = \frac{\lambda}{(1 + t)(\lambda + t)} \quad (10)$$

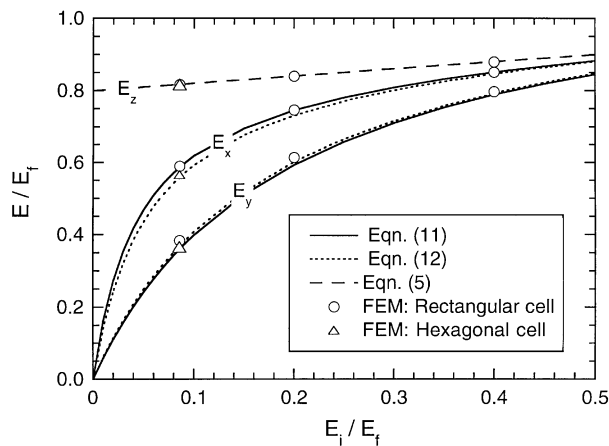


Fig. 7. Comparisons of the analytical solutions for elastic moduli (lines) and those obtained from finite element calculations (symbols) for a unidirectional FM.

This composite sub-cell is then combined with the remaining interphase sub-cell I_1 and the Young's moduli of the entire cell obtained from the Voigt and Reuss averages (as before), yielding the results:

$$\frac{E_x}{E_f} = \frac{\beta(\lambda + t)(1 + \beta t)}{t(1 + \beta t) + \beta\lambda(1 + t)} \quad (11a)$$

and

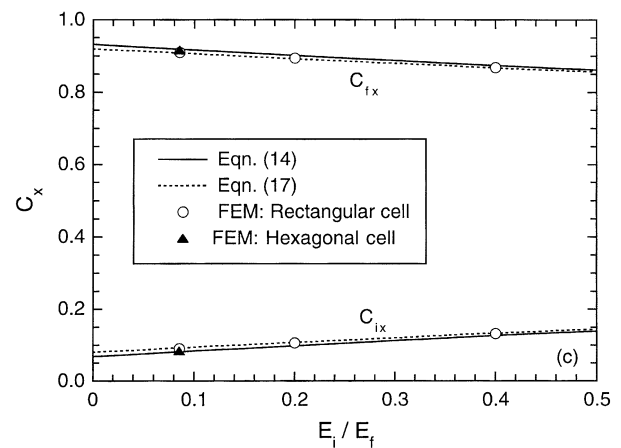
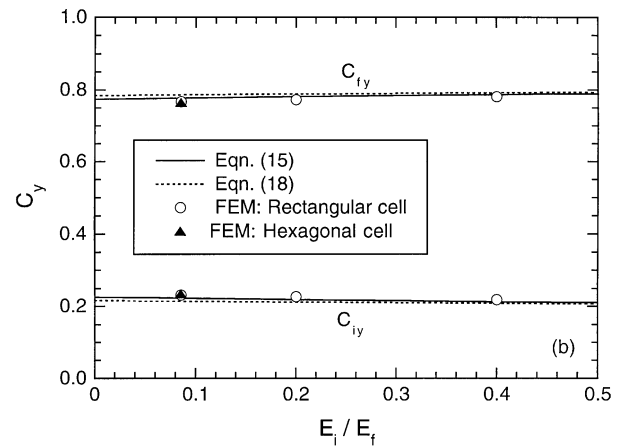
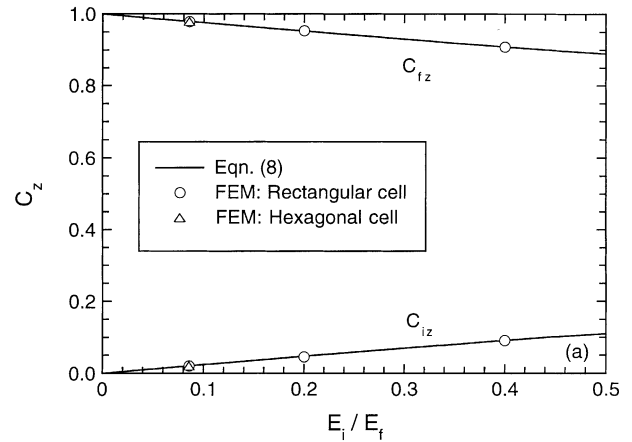


Fig. 8. Coefficients dictating the thermal expansion coefficients for the unidirectional FM in (a) z -direction, (b) y -direction and (c) x -direction.

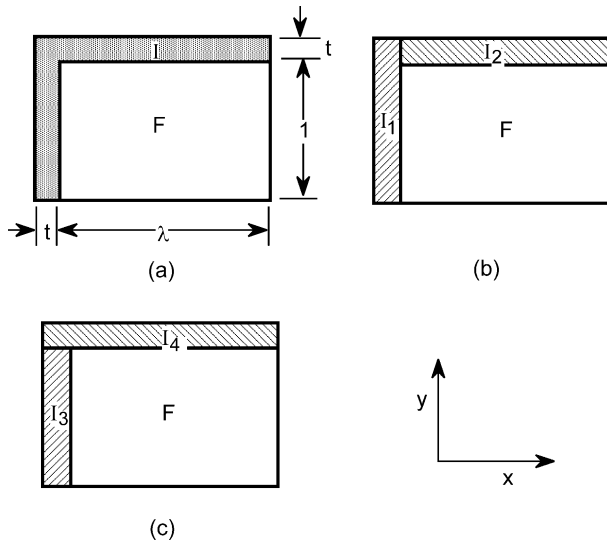


Fig. 9. Schematic showing the subdivision of the unit cell into rectangular slabs.

$$\frac{E_y}{E_f} = \frac{\beta t(\beta + t) + \lambda \beta(1 + t)}{(\lambda + t)(\beta + t)} \quad (11b)$$

Because of the way in which this averaging is performed, it is expected that the results in Eqs. (6) and (7) represent lower bounds to the actual values.

Fig. 9(c) shows an alternate way to subdivide the unit cell. In this case, the fiber, F , is first combined with the interphase sub-cell labeled I_3 and the properties of the composite sub-cell obtained in the manner described above. This composite sub-cell is then combined with the remaining interphase sub-cell, I_4 . Following this procedure, the Young's moduli of the entire composite cell are found to be:

$$\frac{E_x}{E_f} = \frac{\beta t(t + \beta \lambda) + \beta(\lambda + t)}{(t + \beta \lambda)(1 + t)} \quad (12a)$$

$$\frac{E_y}{E_f} = \frac{\beta(1 + t)(\beta t + \lambda)}{t(\beta t + \lambda) + \beta(\lambda + t)} \quad (12b)$$

Again Eqs. (12a) and (12b) are expected to yield lower bound estimates.

Comparisons between the predictions of Eqs. (11) and (12) and the FEA results are shown in Fig. 7. For the range of properties studied here, the correlation between the two sets of results is good, with the difference being consistently $< 5\%$. Furthermore, the analytical results lie slightly below the exact results for the rectangular cell, consistent with the expectation that the former should yield lower bound estimates. The FEA results for the hexagonal cell with $k = 0.35$ and Young's moduli of the $\text{Si}_3\text{N}_4/\text{BN}$ FMs are also included in Fig. 7. The differences in moduli between the two cell shapes is $< 5\%$, demonstrating the insensitivity of the CTE to the

cell shape (at least over the range of shapes applicable to the two FMs studied here).

A similar approach (involving subdivision of the unit cell) is used to obtain the CTEs. Following the scheme shown in Fig. 9(b), the coefficients in the x - and y -directions for the composite sub-cell comprising F and I_2 are:

$$\alpha_x^B = \frac{\beta t}{1 + \beta t} \alpha_i + \frac{1}{1 + \beta t} \alpha_f \quad (13a)$$

$$\alpha_y^B = \left(\frac{t}{1 + t} + \frac{2\nu t(1 - \beta)}{(1 + t)(1 + t\beta)} \right) \alpha_i + \left(\frac{1}{1 + t} - \frac{2\nu t(1 - \beta)}{(1 + t)(1 + t\beta)} \right) \alpha_f \quad (13b)$$

Then, upon combining this composite sub-cell with the sub-cell I_1 , the coefficients for the entire unit cell become:

$$\alpha_x = \left(\frac{t}{\lambda + t} + \frac{\lambda \beta t}{(\lambda + t)(1 + \beta t)} + \frac{2\nu \gamma_B}{1 + \beta t} \right) \alpha_i + \left(\frac{\lambda}{(\lambda + t)(1 + \beta t)} - \frac{2\nu \gamma_B}{1 + \beta t} \right) \alpha_f \quad (14)$$

$$\alpha_y = \left[\frac{t(\beta + t) + \lambda t + \frac{2\nu t(1 - \beta)\lambda}{(1 + t\beta)}}{t(\beta + t) + (1 + t)\lambda} \right] \alpha_i + \left[\frac{\lambda - \frac{2\nu t(1 - \beta)\lambda}{(1 + t\beta)}}{t(\beta + t) + (1 + t)\lambda} \right] \alpha_f \quad (15)$$

where

$$\gamma_B = \frac{\lambda t(1 - \beta)}{[(1 + t)\lambda + t(1 + t\beta)](\lambda + t)} \quad (16)$$

Similarly, for the partitioning scheme shown in Fig. 9(c), the coefficients are:

$$\alpha_x = \frac{1}{t(t + \beta \lambda) + (\lambda + t)} \left[\left(t(t + \beta \lambda) + t + \frac{2\nu \lambda t(1 - \beta)}{(t + \beta \lambda)} \right) \alpha_i + \left(\lambda - \frac{2\nu \lambda t(1 - \beta)}{(t + \beta \lambda)} \right) \alpha_f \right] \quad (17)$$

$$\alpha_y = \left(\frac{t(\beta t + \lambda) + \beta t}{(1 + t)(\beta t + \lambda)} + \frac{2\nu \lambda^2 t(1 - \beta)}{(1 + t)(\beta t + \lambda)[(\beta \lambda + t)t + t + \lambda]} \right) \alpha_i + \left(\frac{\lambda}{(1 + t)(\beta t + \lambda)} - \frac{2\nu \lambda^2 t(1 - \beta)}{(1 + t)(\beta t + \lambda)[(\beta \lambda + t)t + t + \lambda]} \right) \alpha_f \quad (18)$$

By analogy to Eq. (7), it is convenient to re-write the CTEs in the form:

$$\alpha_x = C_{ix}\alpha_i + C_{fx}\alpha_f \tag{19}$$

$$\alpha_y = C_{iy}\alpha_i + C_{fy}\alpha_f \tag{20}$$

where C_{iy} and C_{fy} represent the respective contributions from the interphase and fiber to the CTE in the y -direction, and C_{ix} and C_{fx} are the corresponding values for the CTE in the x -direction. These are obtained readily from Eqs. (14), (15), (17) and (18).

Comparisons between the analytical models and the FEA results for the transverse CTEs of the unidirectional lamina within the cross-ply FM are shown in Fig. 8(b) and (c). Excellent agreement is obtained in all cases, providing confidence in the analytical approach. Because of this correlation, all subsequent comparisons with experimental measurements are based on the analytical models.

For the *cross-ply* FM, material symmetry dictates that the CTE will be isotropic in the plane of hot pressing. The in-plane CTE can be derived readily using the preceding results for the *unidirectional* lamina combined with classical lamination theory. For this purpose, the in-plane strains in each of the laminae are partitioned into thermal and mechanical terms (the latter arising from the anisotropy of the CTE), the strains are set equal to one another to maintain compatibility between adjoining laminae, and the mechanical strains are prescribed in such a way that internal stresses are self-equilibrating. The final result for the in-plane CTE is

$$\alpha_z^c = \alpha_x^c = \alpha_z + \frac{(1 + \nu)(\alpha_x - \alpha_z)}{1 + E_z/E_x + 2\nu} \tag{21}$$

Comparisons between this result and the 3D FEA calculations are presented in Fig. 10, for values of elastic constants applicable to the $\text{Si}_3\text{N}_4/\text{BN}$ FMs and for a range of values of the CTE mismatch, α_i/α_f . The two are in very good agreement.

The predicted through-thickness CTE of the cross-ply material is identical to that of the unidirectional material,

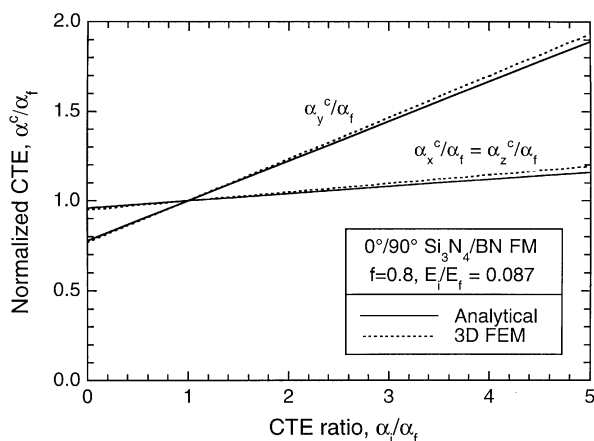


Fig. 10. CTE predictions for cross-ply FM.

given by Eqs. (15) and (18). Similarly good agreement is obtained between this model and the three-dimensional FEA calculations, as shown in Fig. 10.

5. Comparisons between theory and experiment

The analytical models for CTE (Section 4) have been used to predict the CTE of both 0° and $0^\circ/90^\circ$ FMs

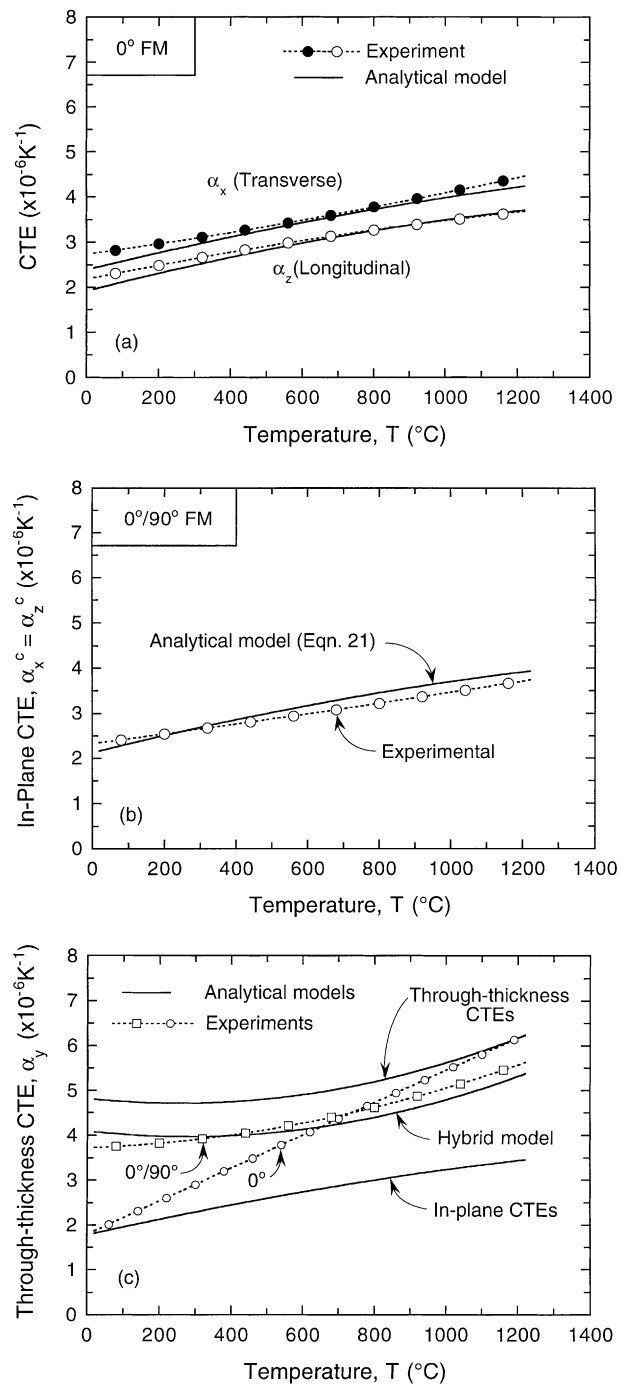


Fig. 11. Comparisons between the measured and predicted CTEs: (a, b) in-plane and (c) through-thickness.

using the appropriate constituent properties and the results have been compared with the experimental measurements on the FMs (Section 3). The key results are plotted in Fig. 11. For the in-plane properties, the relevant constituent properties (CTE and E) were those measured on the neat Si_3N_4 and BN in the in-plane orientation. Very good agreement is obtained between the calculated and measured values. For the through-thickness properties, calculations are presented for two limiting cases: (i) using the *in-plane* properties of both constituents [lower line in Fig. 11(c)]; and (ii) using the *through-thickness* properties of both constituents [upper line in Fig. 11(c)]. These two sets of results appear to bound the experimental data. The results from a hybrid model that accounts for the anisotropy of the constituents in a rudimentary way is also shown in Fig. 11(c) (middle line). The latter model is based on the unit cell sub-division scheme shown in Fig. 9(b). In this case, the CTE values for the fiber and the interphase sub-cell I_2 are taken to be those measured in the through-thickness orientation whereas the CTE of the interphase sub-cell I_1 is taken to be that measured in-plane (assuming that the *c*-axis of the BN crystals is aligned circumferentially around the Si_3N_4 fiber). This approach yields a predicted CTE that agrees better with the experimental data than does either of the two preceding limiting cases, especially in comparison with the $0^\circ/90^\circ$ FM.

6. Summary

Analytical models for the CTE of FMs have been developed, taking into account the fiber shape and the fiber architecture. The models have been validated through the use of finite element calculations. Further validation of the models has been accomplished through comparisons between the model predictions and the experimental measurements. The correlations between theory and experiment appear to be good. Some uncertainty remains with regard to the degree of texturing (especially of the BN) and its effect on the properties of the FMs. This texturing does not appear to have a large influence on the in-plane CTE of either the 0° or $0^\circ/90^\circ$ FMs, provided that the in-plane CTEs of the constituents are used in the models. In contrast, the through-thickness CTE is sensitive to the selection of

the CTE of the BN, since the BN is the “continuous phase” in this orientation and thus plays a more significant role in the CTE of the FM. A rudimentary modification to the model to account for texturing and anisotropy of the BN appears to yield adequate results, although further work is needed to ascertain the extent of texturing and its effect on various thermo-mechanical properties of FMs.

Acknowledgements

Funding for this work was provided by the US Department of Energy (Prime Contract No. W-31-109-Eng-98) to the Argonne National Laboratory and by a subcontract from the Argonne National Laboratory to the University of California, Santa Barbara (Contract No. 981752401). The authors gratefully acknowledge Advanced Ceramics Research for the provision of the materials used in this study, Dr. S. Dorris for helpful discussion on the thermal expansion measurements, and Drs. K. Goretta and W. Coblentz for support and helpful comments.

References

- [1] Mulligan A, Advanced Ceramics Research, private communication.
- [2] Kovar D, King BH, Trice RW, Halloran JW. Fibrous monolithic ceramics. *J Am Ceram Soc* 1997;80(10):2471–87.
- [3] Goretta KC, Singh D, Cruse TA, Ellingson WA, Picciolo JJ, Polzin B, et al. Development of advanced fibrous monoliths: final report for projects of 1998–2000. ANL 01/04, Argonne National Laboratory, June 2001.
- [4] McNulty JC, Begley MR, Zok FW. In-plane fracture resistance of a cross-ply fibrous monolith. *J Am Ceram Soc* 2001;84:367–75.
- [5] Evans AG, Zok FW. The physics and mechanics of fibre-reinforced brittle matrix composites. *J Mater Sci* 2001;84:3857–96.
- [6] Ceramic source, vol. 6. Westerville (OH): Am. Ceram. Soc.; 1990 p. 355.
- [7] Lienard SY, Kovar D, Moon RJ, Bowman KJ, Halloran JE. Texture development in $\text{Si}_3\text{N}_4/\text{BN}$ fibrous monolithic ceramics. *J Mater Sci* 2000;35:3365–71.
- [8] Edgar JH. Crystal structure, mechanical properties, and thermal properties of BN. In: Edgar JH, editor. Properties of group III nitrides. p. 7–21. London: INSPEC; 1994.
- [9] Trice RW, Halloran JW. Investigation of the physical and mechanical properties of hot-pressed boron nitride/oxide composites. *J Am Ceram Soc* 1999;82:2563–5.